Rheol Acta (2016) 55:197–214
DOI 10.1007/s00397-015-0908-1

ORIGINAL CONTRIBUTION

A comparative numerical study of time-dependent structured fluids in complex flows

J. Esteban López-Aguilar[1] · **Michael F. Webster**[1] · **Hamid R. Tamaddon-Jahromi**[1] · **Octavio Manero**[2]

Received: 27 July 2015 / Revised: 26 November 2015 / Accepted: 26 December 2015 / Published online: 29 January 2016

Abstract This study is concerned with the modelling of thixotropic and viscoelastoplastic material systems, contrasting two approaches in the development of such constitutive models. Accordingly, departure from Oldroyd-B-like behaviour is engineered through, first, a new micellar viscoelastic–thixotropic model ($NM\_\tau_p\_ABS$), under the Bautista–Manero framework, and second, a De Souza model. This $NM\_\tau_p\_ABS$ model, is based on the *energy dissipated* by a micellar material to change its internal structure, whilst equivalently, the De Souza model employs the *second invariant of stress*. These models are compared and contrasted in their response through counterpart numerical solutions for axisymmetric contraction–expansion flow. Here, solution features of yielded–unyielded regions, total pressure drop, stress fields and vortex dynamics are analysed under scaling based on the *second-Newtonian viscosity-plateau* (η_s). With the $NM\_\tau_p\_ABS$ model, yield-stress features are identified through solvent-fraction β-variation. In contrast, for the De Souza model, counterpart yield-stress features are exposed through yield-stress τ_{0d}-variation. With either yield-stress increase or rise in elasticity, $NM\_\tau_p\_ABS$ solution response appears *symmetrical* about the contraction-plane axis, whilst *De Souza* patterns prove *asymmetrical*. Under solvent-fraction *decrease*, $NM\_\tau_p\_ABS$ response provides yielded-region shrinkage, upstream and downstream vortex suppression, and non-zero N_1-region growth. Moreover, under *elasticity rise*, fading non-zero N_1-regions, size-invariant yield-fronts and non-zero N_1-regions are observed. In contrast under τ_{0d} increase or rise in *elasticity*, *De Souza* solutions manifest enhancement in vortex activity, and non-zero N_1-region-intensification and expansion. Furthermore, τ_{0d}-rise provokes De Souza yielded-region shrinkage, whilst elasticity does the opposite. On total pressure drop (Δp), for $NM\_\tau_p\_ABS$ and with polymeric-fraction increase at fixed *Wi*, both monotonic rise at low-*Wi* and decline at higher-*Wi* are gathered. In contrast, only a monotonic rising trend is recorded with *De Souza* Δp-solutions for fixed *Wi* under τ_{0d}-rise. Furthermore, with *Wi*-rise and at any fixed $\tau_{0\text{eff}}$-level, both models concur in a declining Δp-trend.

Keywords Yield fronts · Yield stress · Wormlike micelles · Bautista–Manero and De Souza models · Hybrid finite element/volume method · Enhanced oil-recovery · Thixotropy

Introduction

This study addresses the topic of modelling complex flow of viscoelastoplastic fluids in the axisymmetric 4:1:4 contraction–expansion benchmark flow problem. Here, two thixotropic viscoelastic models are considered, both capable of displaying plastic behaviour, the *$NM\_\tau_p\_ABS$ model* (López-Aguilar et al. 2014, 2015a) and the *De Souza model* (De Souza 2011; De Souza 2009). The former, *$NM\_\tau_p\_ABS$ model* (López-Aguilar et al. 2014, 2015a), is based on the Bautista–Manero constitutive modelling approach (Bautista et al. 1999; Manero et al. 2002; Boek et al. 2005). This family of time-dependent thixotropic viscoelastoplastic fluids drive the non-linear non-Newtonian features based the energy dissipated by the

✉ Michael F. Webster
M.F.Webster@swansea.ac.uk

[1] Institute of Non-Newtonian Fluid Mechanics, Swansea University, College of Engineering, Bay Campus, Fabian Way, Swansea SA1 8EN, UK

[2] Instituto de Investigaciones en Materiales, UNAM, 04510 Mexico, Mexico

fluid in a structure equation (via $\boldsymbol{\tau}_p : \boldsymbol{D}$). Here, construction and destruction of the fluid's structure is accounted for in an extra equation for the *f*-functional, which explicitly includes the viscoelasticity (through the relaxation time λ_1 or the Weissenberg number *Wi*) for the NM_τ_p_ABS version. Moreover, relatively low-solvent fractions and high-elasticity levels are accessible. This is achieved through a correction to the constitutive equation for these polymeric Bautista–Manero models, based on physical arguments for fluidity, in which absolute values of the dissipation function are adopted in complex flow (López-Aguilar et al. 2015a). In contrast, the second thixotropic model considered is that constructed by *De Souza* (De Souza 2011; De Souza 2009), which bases its non-linear behaviour on the second invariant of polymeric stress, presented through an additional differential equation for a structure parameter λ. Similarly to the Bautista–Manero models, this De Souza structure equation involves construction and destruction terms, but it is devoid of explicit reference to viscoelasticity (via λ_1 or *Wi*).

Constitutive models

Many approaches have been pursued to model wormlike micelle flow behaviour. A family of models, originating from the Bautista–Manero–Puig (BMP) model (Bautista et al. 1999; Manero et al. 2002), consist of an upper-convected Maxwell constitutive equation for stress-evolution, coupled to a kinetic equation for structural change. Such structural change is flow-induced, involving construction–destruction and is based on the fluidity and rate of energy dissipation. This model can represent viscoelastoplastic characteristics in the limiting ideal-state of infinite zero-shear viscosity (Calderas et al. 2013). In a first reformulation, the modified Bautista–Manero (MBM) model was proposed by Boek et al. (2005), specifically to circumvent the BMP unbounded extensional viscosity predictions. This reformulation was achieved through stress-splitting and fluidity-elimination from the destruction component of the structure equation. More recently, a variant of such micellar models has been proposed that interconnects viscoelasticity with the mechanical structure construction–destruction mechanism (López-Aguilar et al. 2014, 2015a). This variant model deals with MBM-solution anomalies in the Stokesian limit for enhanced pressure drop (*epd*) estimation in contraction–expansion flow (López-Aguilar et al. 2014) and viscosity estimation across the flow field. Most significantly, this model is also able to capture highly-elastic solutions in complex flow (López-Aguilar et al. 2015a). In addition, two variants for this model have been proposed—with energy dissipation given by the following: (i) only the polymer contribution (NM_τ_p model) and (ii) polymer and solvent contributions combined (NM_T model). Such considerations introduce novel physics into the representation, by explicitly coupling the thixotropic and elastic nature of these fluids, alongside new key rheological characteristics, viz. declining first normal stress difference in simple shear flow (López-Aguilar et al. 2014).

In the context of viscoelastoplastic materials, an alternative thixotropic–viscoelastoplastic model was proposed by (De Souza 2011; De Souza 2009), in which non-linear non-Newtonian features are introduced in the destruction-term of the structure equation, dependent upon the second invariant of extra-stress. In a subsequent model-variant published by De Souza and Thompson (2013), such an invariant contribution is taken as unity. This second De Souza model-version has been shown to be capable of displaying *both apparent* and *true* yield-stress response. This particular constitutive equation has been used effectively, in ideal simple and complex flow situations, to represent thixotropic and viscoelastoplastic characteristics; *see for example*, an overview of models representing viscoelastoplasticity (De Souza and Thompson 2012); and flow in an expansion setting (Link et al. 2015).

Applications

The Bautista–Manero constitutive equation was originally devised to model a versatile family of fluids composed of mixtures of surfactants—typically of cetyltrimethylamonium bromide (CTAB), or cetylpyridinium chloride (CPyCl)—and salts, sodium salicylate (NaSal), in water (Bautista et al. 1999; López-Aguilar et al. 2014; Yang 2002). These components interact physically to form elongated micelles, the rate of which formation depends upon concentration, temperature and pressure conditions. These micelle networks entangle and provoke changes in viscosity, elasticity, and breakdown-formation of internal structure (López-Aguilar et al. 2014, 2015a). Such complex system constitution generates highly complex rheological phenomena, which manifest features associated with thixotropy (Bautista et al. 1999), pseudo plasticity (Bautista et al. 1999; Manero et al. 2002; Boek et al. 2005; López-Aguilar et al. 2014, 2015a), shear banding (Bautista et al. 2000) and yield stress (Calderas et al. 2013; López-Aguilar et al. 2015b). Advantage may be taken of these features to render micelle solutions as 'smart-fluids' for varied processing and present-day applications—as in, drilling fluids for enhanced oil-reservoir recovery (EOR) (López-Aguilar et al. 2014), and additives in household-products, paints, cosmetics, health-care products, drag reducing agents (López-Aguilar et al. 2014; Yang 2002). In contrast, the De Souza model is intended to model viscoelastoplastic thixotropic materials (De Souza 2009, 2011; De Souza and Thompson 2013), such as those processing fluids used within the oil industry.

The current contraction–expansion flow problem under study is a standard benchmark in experimental and computational rheology (Binding et al. 2006; Aguayo et al. 2008;

Walters and Webster 2003; Rothstein and McKinley 2001). Its commending features relate to its *vortex dynamics* (re-entrant/salient), *stress fields*, *flow kinematics* and *pressure-drop* measurement (López-Aguilar et al. 2014). Here, diverse solution response may be found, relating to vortex dynamics and stress-field evolution (extensional viscosity, N_2-effects), structure formation and numerical tractability (sharp-rounded corners) (Aboubacar et al. 2002a, b). One notes that pressure drop, which reflects the energy expended in a flow, is often studied through total pressure-drop measurement (Binding et al. 2006; Aguayo et al. 2008), the accurate capture of which itself offers a significant challenge to computational prediction (Binding et al. 2006).

Flow problem, modelling and discretisation

In this section, two constitutive approaches for thixotropic viscoelastoplastic fluids are presented. The first of them is conducted via the Bautista–Manero fluid family, for which the NM_τ_p_ABS model (López-Aguilar et al. 2014, 2015a and b) is chosen. This constitutive equation reflects viscoelastoplastic features through solvent-fraction β-variation in the range $10^{-2} \leq \beta \leq 0.9$. In contrast, the De Souza model (De Souza 2011) provides viscoelastoplastic characteristics through yield-stress τ_{0d}-variation in the range $0.02 \leq \tau_{0d} \leq 1$.

The viscosity scaling used in this study is based on the solvent viscosity η_s. Here, polymeric viscosity, stress and pressure dimensionless variables are defined as follows:

$$\eta_p^* = \frac{\eta_p}{\eta_s},\ \boldsymbol{\tau}_p^* = \frac{\boldsymbol{\tau}_p}{\eta_s \frac{U}{L}},\ \boldsymbol{\tau}_s^* = \frac{\boldsymbol{\tau}_s}{\eta_s \frac{U}{L}},\ p^* = \frac{p}{\eta_s \frac{U}{L}},$$

with U being a characteristic velocity scale (mean velocity, based on volume flow rate), and L a spatial-scale (based on minimum contraction-gap width). The dimensionless variables for spatial coordinates, velocity, time and rate-of-deformation are as follows:

$$\boldsymbol{x}^* = \frac{\boldsymbol{x}}{L},\ \boldsymbol{u}^* = \frac{\boldsymbol{u}}{U},\ t^* = \frac{U}{L}t,\ \boldsymbol{D}^* = \frac{L}{U}\boldsymbol{D}.$$

The governing equations under transient, incompressible and isothermal flow conditions may be expressed through those for mass conservation and momentum transport, coupled to a viscoelastic constitutive law for stress. Such a space-time partial differential equation system may be expressed in non-dimensional form as follows:

$$\nabla \cdot \boldsymbol{u} = 0, \tag{1}$$

$$\mathrm{Re}\frac{\partial \boldsymbol{u}}{\partial t} = \nabla \cdot \boldsymbol{T} - Re\boldsymbol{u} \cdot \nabla \boldsymbol{u} - \nabla p, \tag{2}$$

$$\boldsymbol{T} = \boldsymbol{\tau}_s + \boldsymbol{\tau}_p, \tag{3}$$

$$\boldsymbol{\tau}_s = 2\boldsymbol{D}, \tag{4}$$

$$Wi\overset{\nabla}{\boldsymbol{\tau}}_p = 2\Gamma\boldsymbol{D} - f\boldsymbol{\tau}_p. \tag{5}$$

Note, in these governing equations (1–5), the * notation on dimensionless variables is discarded for concise-form representation, retained by implication only. Here, field-dependent variables, $\boldsymbol{u}$, p and $\boldsymbol{T}$, represent fluid velocity, hydrodynamic pressure and total stress contributions; ($\boldsymbol{x}$, t) represent space–time independent variables; and the gradient and divergence operators apply over the spatial domain. The stress ($\boldsymbol{T}$) is split into a solvent (viscous) contribution $\boldsymbol{\tau}_s$, and a polymeric-contribution $\boldsymbol{\tau}_p$ (thixotropic–viscoelastoplastic). In addition, $\boldsymbol{D} = (\nabla\boldsymbol{u} + \nabla\boldsymbol{u}^\dagger)/2$ is the rate of deformation tensor, with tensor transpose superscript notation †.

The Reynolds group number may be defined as $Re = \rho UL/\eta_s$ with ρ representing a material density parameter. In all solutions presented creeping flow approximation is assumed with $Re \leq 10^{-2}$. A dimensionless viscosity ratio $\Gamma = \eta_{p0}/\eta_s$ is obtained in the rhs of constitutive Eq. (5). Here, Γ modulates the dissipative-term contribution to the polymeric stress equation. Moreover, an elastic Weissenberg group number, defined as $Wi = \lambda_1 U/L$, is introduced as a second dimensionless group number, specified through a characteristic material relaxation time, $\lambda_1 = (\eta_{p0}/G_0)$, and a characteristic process rate, U/L. Here, G_0 represents the elastic modulus of the material.

NM_τ_p_ABS model

Next, the generalised functional f in Eq. (5) must be specified, to imbue a thixotropic networked nature to the fluid system. Recently, a new constitutive equation, based on the MBM model, has been proposed for modelling wormlike micellar systems, that of NM_τ_p. This model has the *novel inclusion of viscoelasticity* within the destruction mechanics of the fluid-network structure and corrects for MBM-*epd* undershoot at low deformation rates (López-Aguilar et al. 2014). Moreover, this formulation has been further developed to capture highly-nonlinear solutions in complex flows (López-Aguilar et al. 2015a), at large-Wi or low-β (translating in high polymer concentrations). The present analysis appeals to a sub-version of this class of models, NM_τ_p_ABS, which in addition to the foregoing uses the absolute value of the dissipation function (guaranteeing positive viscosity; López-Aguilar et al. 2015a), and considers *only* the energy dissipated by the *polymer constituent* (τ_p) in the structure breakup. As such, dependency on fluidity ($\phi_p = \eta_p^{-1}$) arises through its equivalent dimensionless structure functional f, of generalised differential form (López-Aguilar et al. 2014, 2015a),

$$\left(\frac{\partial}{\partial t} + \boldsymbol{u} \cdot \nabla\right) f = \frac{1}{\omega}(1-f) + \xi_{G_0}^{\eta_s} Wi \left|\boldsymbol{\tau}_p : \boldsymbol{D}\right|. \tag{6}$$

Here, the dimensionless functional f is defined as $f=(\eta_{p0}/\eta_p)$, using η_{p0} as a viscous scaling factor on fluidity. The dimensionless micellar parameters, which account for structural construction ($\omega=\lambda_s U/L$) and destruction ($\xi_{G_0}^{\eta_s}=kG_0$), appear in Eq. (6), in the corresponding terms for these dynamic mechanisms.

De Souza model

This model consists of a dimensional total-stress form, coupled with a differential equation describing the material structure λ evolution (De Souza 2011). This structure parameter λ explicitly affects the viscosity and shear modulus. To establish a common basis with NM_τp_ABS, the De Souza stress equation is re-written in a split form ($\boldsymbol{T}=\boldsymbol{\tau}_s+\boldsymbol{\tau}_p$). Here, $\boldsymbol{\tau}_s=2\boldsymbol{D}$ and $\boldsymbol{\tau}_p$ are the Newtonian-solvent and non-linear polymeric stress contributions, respectively. Moreover, the polymeric stress equation may be rearranged to obtain:

$$Wi\overset{\nabla}{\boldsymbol{\tau}}_p=2\frac{\Gamma}{\lambda^m}\boldsymbol{D}-f\boldsymbol{\tau}_p, \tag{7}$$

where the f-functional is defined as $f=\frac{1}{\lambda^m}\left(\eta_{p0}/\eta_p\right)$, the polymeric viscosity is $\eta_p(\lambda)=\left(\frac{\eta_{p0}}{\eta_s}\right)^{\lambda}-1$, and structural modulus is $\frac{G_s(\lambda)}{G_0}=\frac{1}{\lambda^m}$. In addition, the structure equation is given by:

$$\left(\frac{\partial}{\partial t}+\boldsymbol{u}\cdot\nabla\right)\lambda=\frac{1}{\omega_{DS}}\left[(1-\lambda)^a+(1-\lambda_{ss})^a\left(\frac{\lambda}{\lambda_{ss}}\right)^b\left(\frac{II_{\boldsymbol{\tau}_p}}{\left[\frac{\eta_p(\lambda)}{\eta_s}+1\right]II_{\boldsymbol{D}}}\right)^c\right]. \tag{8}$$

Here, $\omega_{DS}=t_{eq}U/L$ is a dimensionless time of change of λ; $II_{\boldsymbol{\tau}_p}=\sqrt{\frac{1}{2}tr\boldsymbol{\tau}_p^2}$ and $II_{\boldsymbol{D}}=\sqrt{\frac{1}{2}tr\boldsymbol{D}^2}$ are the second invariants of polymeric stress and rate-of-deformation, respectively; a, b, c and m are dimensionless positive constants. Additionally, the steady-state structure parameter λ_{ss} is defined as:

$$\lambda_{ss}(II_{\boldsymbol{D}})=\frac{\ln\eta_{ss}(II_{\boldsymbol{D}})-\ln\eta_s}{\ln\eta_{p0}-\ln\eta_s}, \tag{9}$$

and the expression for the steady-state viscosity η_{ss} is:

$$\eta_{ss}(II_{\boldsymbol{D}})=\left[1-\exp\left(-\frac{II_{\boldsymbol{D}}}{\tau_0}\right)\right]\left[\frac{\tau_0-\tau_{0d}}{II_{\boldsymbol{D}}}\exp\left(-\frac{II_{\boldsymbol{D}}}{\dot{\gamma}_{0d}}\right)+\frac{\tau_{0d}}{II_{\boldsymbol{D}}}+KII_{\boldsymbol{D}}{}^{n-1}\right]+1. \tag{10}$$

Above, τ_0 and τ_{0d} are the dynamic and static yield-stress parameters, respectively; $\dot{\gamma}_{0d}$ is the shear-rate that marks the transition from τ_0 to τ_{0d}. Finally, K and n are consistency and power law indexes, respectively.[1]

[1] Note, care in solution must be taken numerically with possible zero-variable denominators appearing in Eqs. 7–10, as in $\frac{1}{\lambda^m}$ of Eq. 7, λ_{ss}^{-1} of Eq. 8, and $II_{\boldsymbol{D}}^{-1}$ of Eqs. 8, 10. Here, a simple shift with unity suffices.

Material functions

In Fig. 1, the matching is provided across NM_τp_ABS and De Souza constitutive models for (a) shear (η_{Shear}) and extensional (η_{Ext}) viscosities and (b) shear-stress (τ_{rz}). Here, the solvent-fraction (β) is set to the relatively high polymeric value of 1/9, a frequent benchmark setting. Fluids with moderate hardening features are characterised with NM_τp_ABS parameters of $\{\omega,\ \xi_{G0}\}=\{4.0,\ 1.0\}$ and De Souza parameters of $\{\omega_{DS},\ K,\ n,\ \tau_0,\ \tau_{0d},\ \dot{\gamma}_{0d},\ \beta\}=\{1.0,\ 0.1,\ 0.5,\ 0.2,\ 0.2,\ 0.3,\ 1/9\}$. It may be gathered that insignificant differences are observed across models in η_{Shear}, η_{Ext} and τ_{rz} (Fig. 1a, b). In contrast, first normal stress difference ($N_{1\text{Shear}}$) (Fig. 1c) does display some interesting disparities in the moderate-to-high shear-rate range. There, a plateau is observed in NM_τp_ABS $N_{1\text{Shear}}$ data, as opposed to that provided with the De Souza model, which first undulates at moderate shear rates, manifesting local extrema, to finally rise monotonically at large shear rates. One notes, for instance at $\lambda_1\dot{\gamma}=10^5$, the De Souza $N_{1\text{Shear}}$ level is some six times larger ($N_{1\text{Shear}}\sim 3$) than that of NM_τp_ABS ($N_{1\text{Shear}}\sim 5\times10^{-1}$).

In Fig. 2a–d, shear data is provided in the form of τ_{rz} and $N_{1\text{Shear}}$, where one may compare and contrast the viscoelastoplastic features of both NM_τp_ABS and De Souza models. Overall, NM_τp_ABS τ_{rz}-representation (Fig. 2a) reflects a branched pattern, with its fingers providing effective yield-stress $\tau_{0\text{eff}}$-levels (intercepts of τ_{rz}-curves at $\lambda_1\dot{\gamma}\to0$), whilst equivalently De Souza data curves (Fig. 2c, at expanded scale) render a closed-form shape. Firstly, solvent-fraction β-decrease is used in order to display *NM_τp_ABS* yield-stress features. In Fig. 2a, b, τ_{rz} and N_1 data are plotted under *solvent-fraction β-variation*, with the base thixotropic parameter set of $\{\omega,\ \xi_{G0}\}=\{4.0,\ 1.0\}$ (López-Aguilar et al. 2015b). Here, with β-decrease of $\beta=\{0.9,\ 1/9,\ 10^{-2},\ 10^{-3}\}$, the $\tau_{0\text{eff}}$-level rises through $\tau_{0\text{eff}}=\{0.01,\ 0.1,\ 1.0,\ 10\}$, whilst the high shear-rate $N_{1\text{shear}}$ plateaux elevate through $N_{1\text{Shear}}\sim\{0.4,\ 4,\ 50,\ 500\}$.

In contrast, *De Souza* yield-stress features are exposed through *yield-stress τ_{0d}-variation* (where $\tau_0=\tau_{0d}$). A data sample of τ_{rz} and N_1 is provided in Fig. 2c, d, under parameters sets of $\tau_{0d}=\{0.1,\ 0.2,\ 0.5,\ 1.0,\ 2.0\}$ and $\{K,\ n,\ \dot{\gamma}_{0d},\ \beta\}=\{0.1,\ 0.5,\ 0.3,\ 1/9\}$. Now, De Souza τ_{rz}-curves intercept the vertical-axis as $\lambda_1\dot{\gamma}\to0$ at $\tau_{rz}\sim10^{-1}$ (Fig. 2c). Notably, the $\tau_{0\text{eff}}$-level is dictated by τ_{0d}. This coincides with the location of the *first vertex of the centre of curvature*[2] of each τ_{0d}-curve, as indicated. Subsequently, for moderate shear rates, both NM_τp_ABS and De Souza τ_{rz}-curves decline away from their prior linear slopes. Here, De Souza τ_{0d}-curves appear less flat and smaller in plateau level, than comparably for

[2] In the geometry of planar curves, a vertex is a point where the first derivative of curvature is zero. This is typically a local maximum, a local minimum, or a stationary point of inflection of curvature.

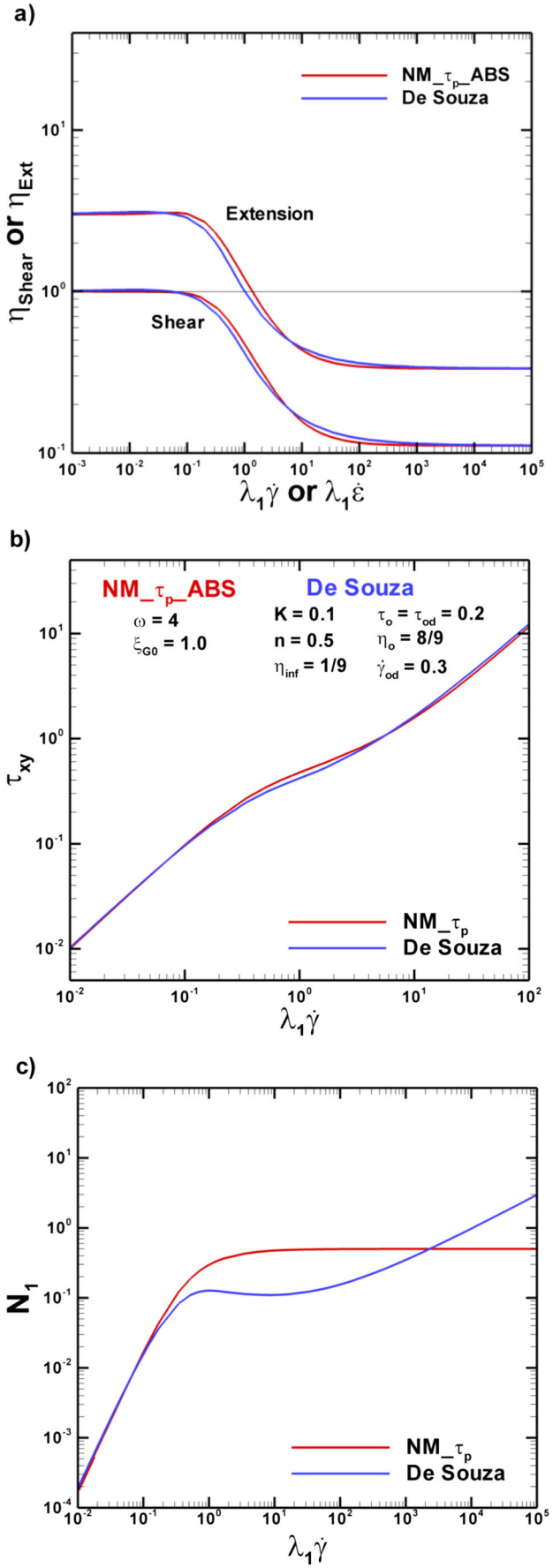

◀ **Fig. 1** Material functions against dimensionless rate. **a** Shear (η_{Shear}) and extensional (η_{Ext}) viscosities. **b** τ_{rz}. **c** N_{1Shear}; $\beta = 1/9$. NM_τ_p_ABS: $\{\omega, \xi_{G0}\} = \{4.0, 1.0\}$, De Souza: $\{K, n, \tau_0, \tau_{0d}, \dot{\gamma}_{0d}, \beta, \omega_{DS}\} = \{0.1, 0.5, 0.2, 0.2, 0.3, 1/9, 1.0\}$

NM_τ_p_ABS response under solvent-fraction decrease. Such De Souza response has fixed width per τ_{0d}-level, of one-and-half decades, covering in total the three-decade rate-range of $10^{-1} \leq \lambda_1\dot{\gamma} \leq 10^2$ for the span of τ_{0d}-values. Note, with rising τ_{0d}, the range of τ_{rz} gradually shifts through larger values. The NM_τ_p_ABS response widens with β-decrease: this range is restricted for $\beta = 1/9$ to $10^0 \leq \lambda_1\dot{\gamma} \leq 5*10^1$ at minimum; whilst for $\beta = 10^{-3}$, the range expands out to $10^0 \leq \lambda_1\dot{\gamma} \leq 10^3$ at maximum. Finally, at larger shear rates, all τ_{rz}-curves re-join, supporting a rising linear trend. In terms of De Souza N_{1Shear}-representation for rising deformation rate, there is initial rise in N_{1Shear}, prior to location of an inflection point at moderate shear rates (Fig. 2d). With τ_{0d}-rise, this inflection point consistently elevates, whilst being shifted to larger shear rates. Beyond this inflection point, these N_{1Shear}-curves decline at moderate-to-high shear rates, to finally rise again at high shear rates.

Counterpart viscous response under NM_τ_p_ABS and De Souza is provided, covering η_{Shear} in Fig. 3a, c and η_{Ext} in Fig. 3b, d. Under β-decrease, NM_τ_p_ABS viscoelastoplastic features are reflected in the low deformation-rate viscosity-plateau levels of Fig. 3a, b. Here, and with $\beta = \{0.9, 1/9, 10^{-2}, 10^{-3}\}$, η_{Shear} and η_{Ext} first-Newtonian viscosity-plateaux elevate, to $\eta_{Shear} = \{1.11, 9, 100, 1000\}$ and $\eta_{Ext} = \{3.33, 27, 300, 3000\}$, respectively. Such viscosity-plateau elevation exaggerates the extent of the drop to the second-Newtonian viscosity-plateau, due to exposure to shear-thinning in η_{Shear} and strain-softening in η_{Ext}. Moreover, the *second-Newtonian* viscosity-plateaux ultimately unite to share a common level $\forall\beta$. In contrast for De Souza in Fig. 3c, d, the initial η_{Shear}- and η_{Ext}-drops are shifted to larger deformation rates with τ_{0d}-rise. Conspicuously, $\tau_{0d} = 1.0$ η_{Ext}-curve is the only instance in which both strain hardening and softening features are captured. Now, as the De Souza solvent-fraction level is fixed at $\beta = 1/9$, the first- and second-Newtonian-viscosity plateaux are common in each viscometric instance considered.

Problem specification and discretisation

The schematic representation of the 4:1:4 axisymmetric, rounded-corner contraction–expansion flow problem, alongside its corresponding mesh data, is reported elsewhere (López-Aguilar et al. 2014; Aguayo et al. 2008). See Aguayo et al. (2008) for further detail on this problem, which provides a full mesh refinement analysis for some typical case studies. Here, the lengths of the inlet and outlet regions are taken as 19.5H, where H is the upstream geometry radius divided by a factor of four. Symmetry is enforced at the centreline. No-slip boundary conditions are enforced on the

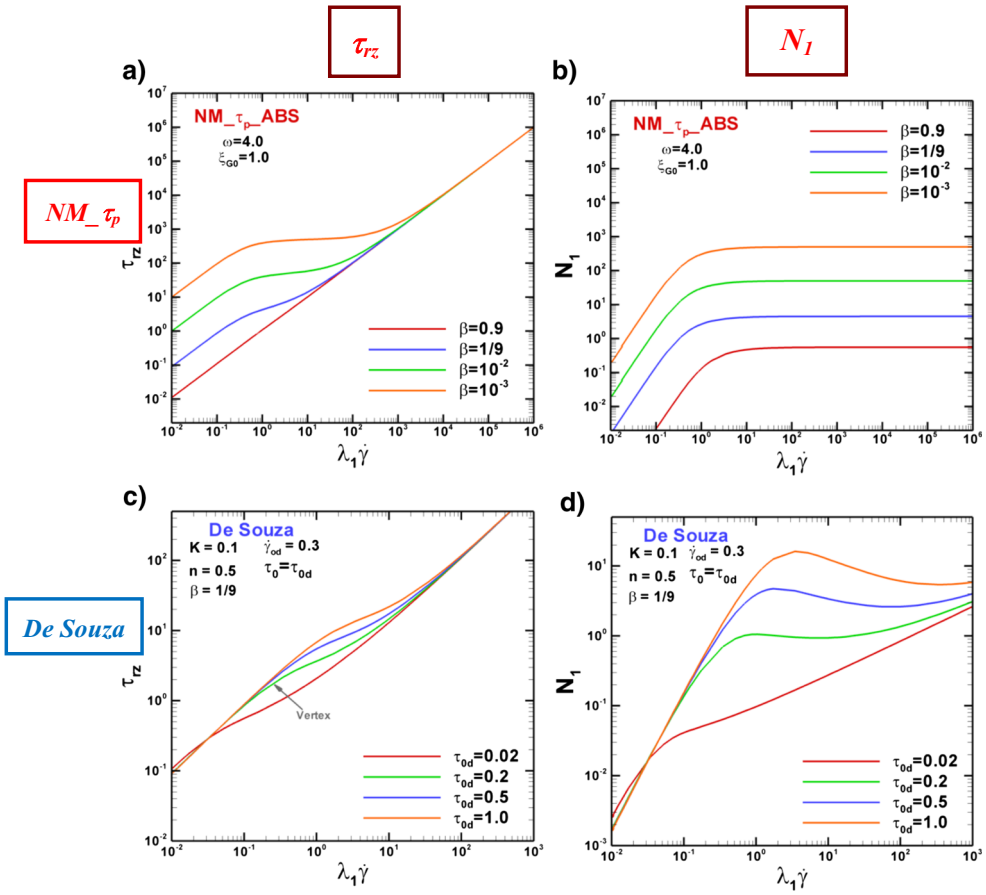

Fig. 2 τ_{rz} and N_{1Shear} against shear-rate; top-NM_τ_p_ABS(β-decrease) $\{\omega, \xi_{G0}\} = \{4.0, 1.0\}$, $\beta = \{0.9, 1/9, 10^{-2}, 10^{-3}\}$; bottom-De Souza($\tau_{0d}$-increase) $\{K, n, \dot{\gamma}_{0d}, \beta, \omega_{DS}\} = \{0.1, 0.5, 0.3, 1/9, 1.0\}$, $\tau_{0d} = \{0.1, 0.2, 0.5, 1.0, 2.0\}$

bounding wall. Entry flow kinematics is determined computationally for the equivalent entry-channel problem. These may be imposed through the time-stepping procedure, either as steady-state, or via a smooth transient build-up. Then, fully developed outflow conditions are established ensuring no change in streamwise and vanishing cross-stream kinematics. Once fully developed entry flow kinematic is known, stress may be determined in a pointwise fashion through the derived corresponding ODE system for stress.

Hybrid finite element/finite volume scheme

The discrete method of approximation is that of a hybrid finite element/volume scheme, as used elsewhere (Matallah et al. 1998; Belblidia et al. 2008; Webster et al. 2005, Wapperom and Webster 1998). Such a scheme is a semi-implicit, time-splitting, fractional three-staged formulation, which draws upon finite element discretisation for velocity-pressure approximation and cell-vertex finite volume discretisation for stress. This scheme combines the individual advantages and benefits offered by each approach (see Matallah et al. 1998; Belblidia et al. 2008; Webster et al. 2005, Wapperom and Webster 1998). A sub-cell cell-vertex *fv*-scheme is implemented for extra-stress, founded upon fluctuation-distribution for fluxes (upwinding) and median-dual-cell treatment for source terms. In addition, Galerkin *fe*-discretisation is imposed on the embedded Navier–Stokes system components; the momentum equation at stage-1, the pressure-correction equation at stage-2 and the incompressibility satisfaction constraint at stage-3 (to ensure higher order precision). The sub-cell *fv*-triangular-tessellation is then constructed from the parent *fe*-triangular-grid by connecting the mid-side nodes. Such a tessellation is structured in nature. Stress variables are located at the vertices of *fv*-sub-cells (cell-vertex method, equivalent to linear interpolation). In contrast, quadratic velocity interpolation is enforced on the parent *fe*-cell, alongside linear pressure interpolation. A direct Choleski solution method is utilised for the *fe* pressure-correction stage-2; whilst for velocity-stages (1,3) under *fe*-components, a space-efficient element-by-element Jacobi iteration is chosen.

Vortex dynamics results: (a) NM_τ_p_ABS, β and *Wi*-variation

In Fig. 4a, NM_τ_p_ABS streamline patterns are displayed, with solvent concentration (β) decrease and elasticity (*Wi*)

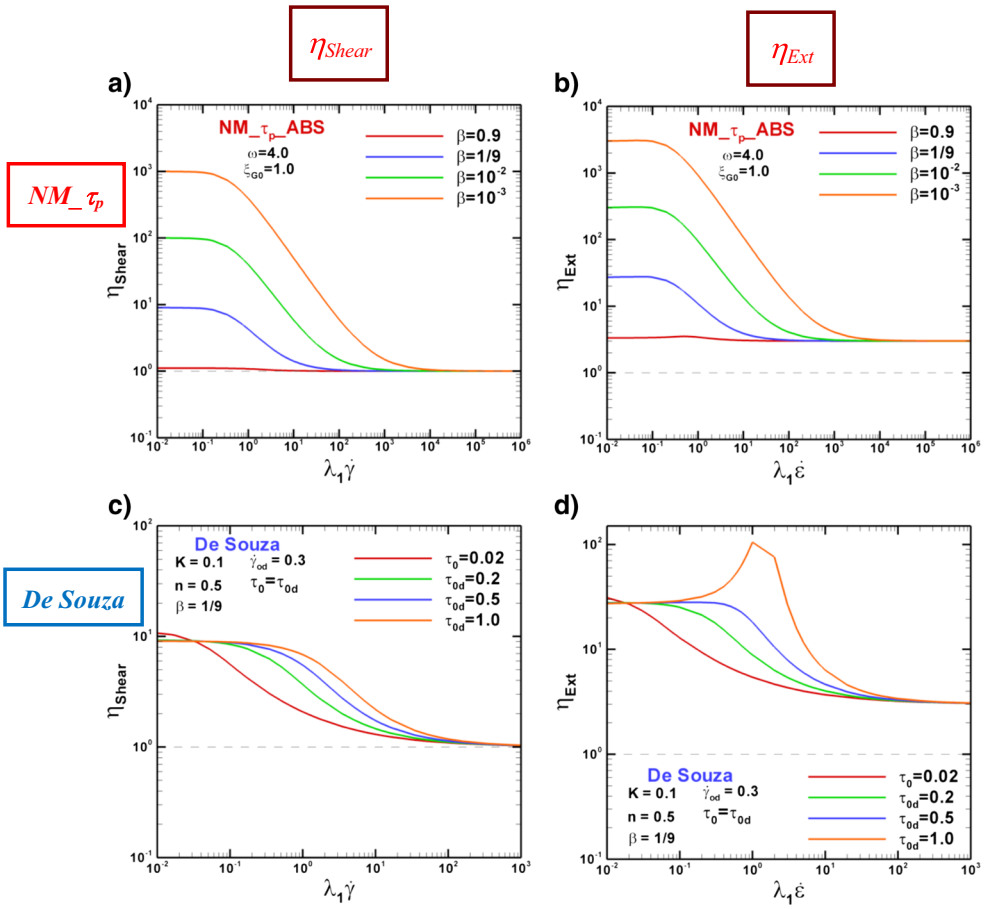

Fig. 3 η_{Shear} and η_{Ext} against deformation-rate; top-NM_τ_p_ABS(β-decrease) $\{\omega, \xi_{G0}\} = \{4.0, 1.0\}$, $\beta = \{0.9, 1/9, 10^{-2}, 10^{-3}\}$; bottom-De Souza($\tau_{0d}$-increase) $\{K, n, \dot{\gamma}_{0d}, \beta, \omega_{DS}\} = \{0.1, 0.5, 0.3, 1/9, 1.0\}$, $\tau_{0d} = \{0.1, 0.2, 0.5, 1.0, 2.0\}$

increase. Such data are analysed: (i) by observing the effects on streamline patterns of adjustment in polymer concentration at fixed elasticity (*Wi*) levels; and likewise, (ii) through the effects of elasticity increase at fixed solvent-fraction level.

For *β-decrease at fixed Wi* = 1 (where elastic and viscous stresses balance), vortex suppression (upstream–downstream) is observed as polymer concentration is elevated. Hence, at *Wi* = 1, evolution is observed from two well-developed upstream and downstream vortices at $\beta = 0.9$, to vortex removal at $\beta = 1/9$; see vortex intensity values in Table 1 and *upstream–downstream* vortex-intensity trend graphs in Fig. 4b–e. Such vortex suppression correlates with relatively stronger yield-stress features as polymer concentration increases. These are reflected in larger τ_{0eff}, τ_{rz}- and N_{1Shear}-plateaux with β-decrease (Fig. 2a, b), in addition to larger η_{Shear} and η_{Ext} first-Newtonian viscosity-plateaux (Fig3a, b). At higher elasticity levels ($Wi = \{5, 10\}$), such trends in vortex suppression are still further amplified, whilst also displaying asymmetry in size about the contraction. In contrast to *Wi* = 1 states, as elasticity is decreased to *Wi* = 0.1 and at each β-level, vortices recover greater strength and size, and upstream–downstream symmetry is even more apparent.

Under *Wi-variation at fixed (β) polymer concentration*, the additional data of vortex-intensity trend graphs (in Fig. 4b, c, plotted against (1-β) for consistency in trend direction across model comparison; or against *Wi,* in Fig. 4d, e), reveal the strong fall-off in intensity between $1/9 \leq \beta \leq 0.5$, which becomes more exaggerated with *Wi*-rise. This aspect is present in both upstream and downstream vortex response. In viscometric flows, this vortex intensity loss may be correlated through deformation-rate rise, with the prominent drop in η_{Shear}- and η_{Ext}-data of Fig. 3a, b. Here, the η_{Shear}-decline may be attributed to the prevailing shear-thinning, whilst the η_{Ext}-drop is due to strain-softening. Note also, at $\beta = 0.5$, there is both vortex-suppression and some slight enhancement. In *upstream vortex activity*, three different phases of response may be identified over $Wi = \{0.1, 1.0, 5.0, 10.0\}$: *(phase-one, high-solvent, $\beta = 0.9$)*, only vortex-enhancement; *(phase-two, medium-solvent, $\beta = 0.5$)*, a first stage of vortex-suppression for $0.1 \leq Wi \leq 5$; followed by vortex-enhancement for $5 \leq Wi \leq 10$; and *(phase-three, high-solute, $\beta = \{0.3, 1/9\}$)*, where only vortex-suppression is observed (see Table 1, Fig. 4d). Notably, at $\beta = 1/9$ *high-solute* level, no vortex structures can be graphically distinguished for $Wi \geq 1.0$. *Downstream vortex activity* (Fig. 4e), rather mirrors the upstream response, bar the final-*Wi* stages at $\beta = 0.3$, where suppression is stronger in the upstream case. Such observations of trends in vortex inhibition are consistent with our prior

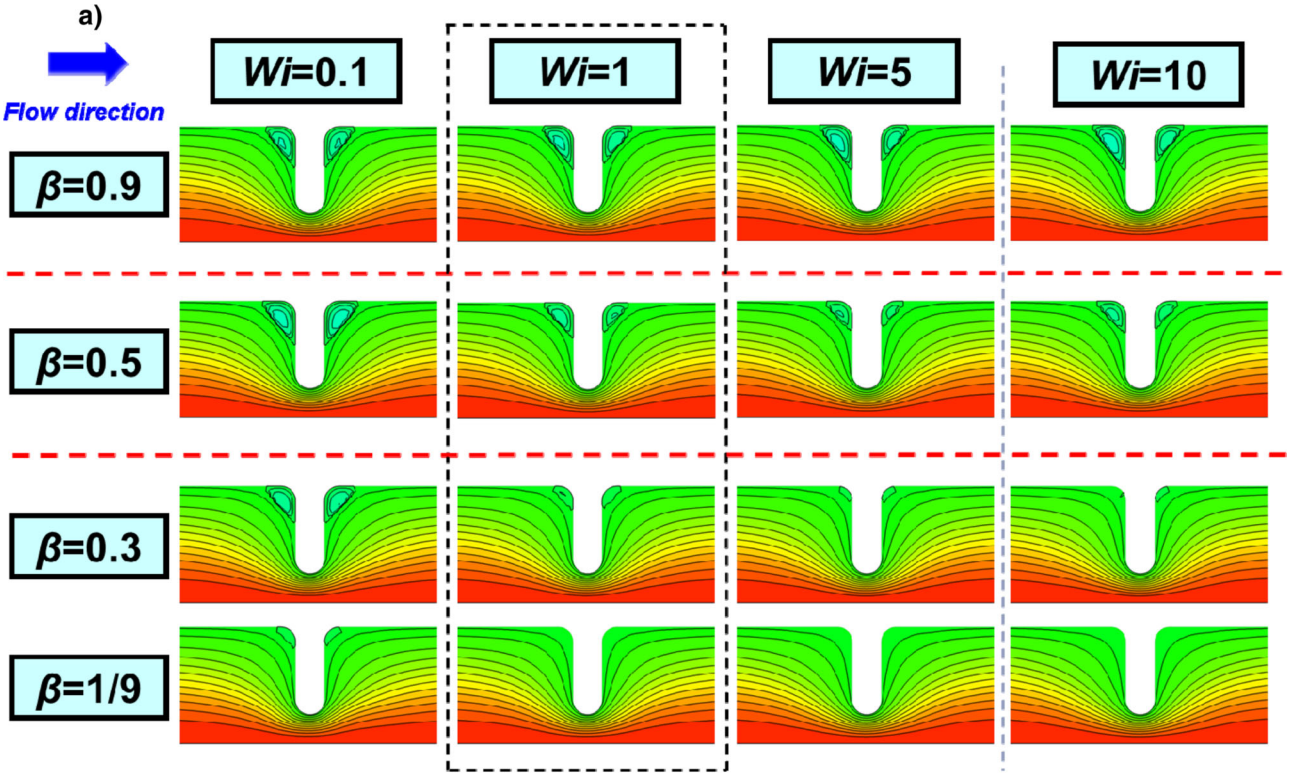

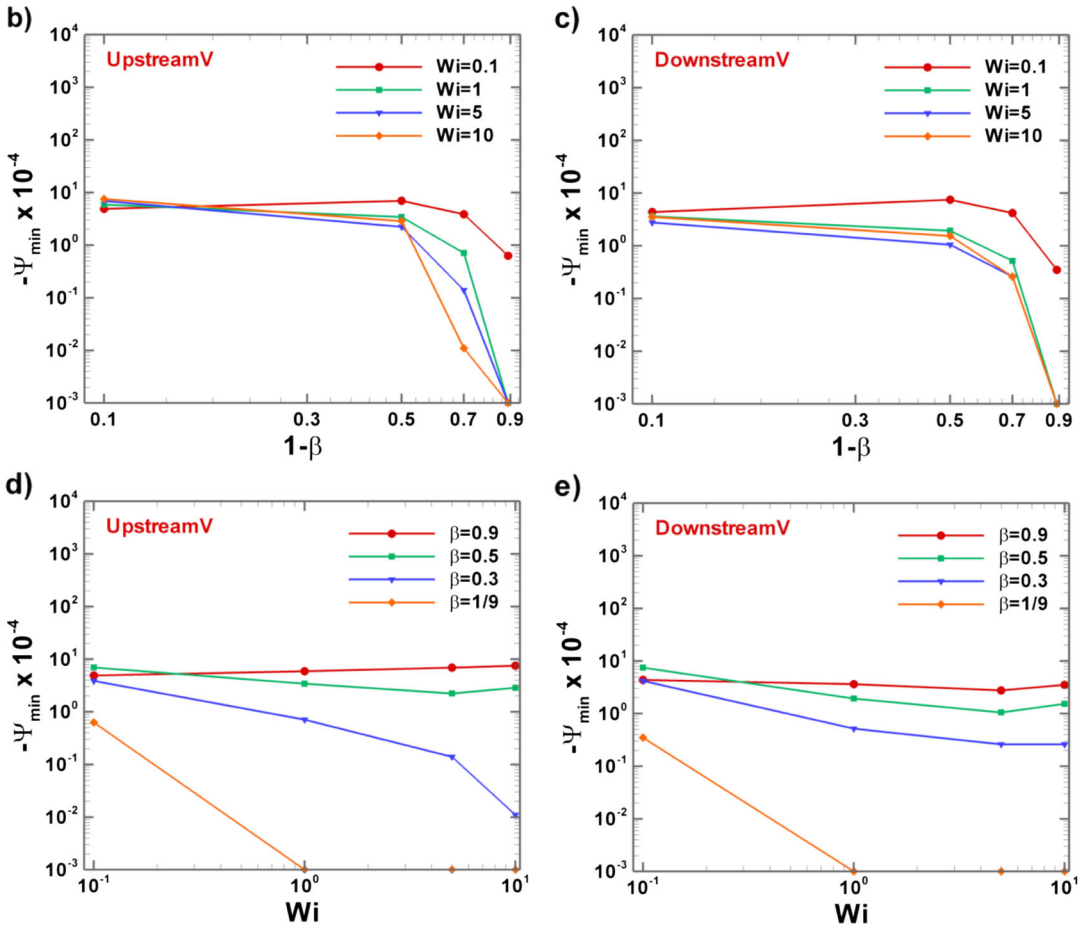

Fig. 4 Streamlines and vortex intensity against β and *Wi*; NM_τ_p_ABS $\{\omega, \xi_{G0}\} = \{4.0, 1.0\}$ β-variation $\beta = \{0.9, 0.5, 0.3, 1/9\}$

Table 1 Vortex intensity ($\Psi_{min} = -\Psi_{min}^{*}\ x10^{-4}$) against β and Wi; NM_τ_p_ABS $\{\omega, \xi_{G0}\} = \{4.0, 1.0\}$

	$\Psi_{min} = -\Psi_{min}^{*}\ x10^{-4}$							
	$Wi = 0.1$		$Wi = 1.0$		$Wi = 5.0$		$Wi = 10.0$	
β	Ups	Dns	Ups	Dns	Ups	Dns	Ups	Dns
0.9	4.89	4.36	5.92	3.62	6.91	2.76	7.55	3.52
0.5	6.94	7.48	3.43	1.94	2.23	1.05	2.87	1.54
0.3	3.86	4.20	0.71	0.52	0.14	0.26	0.011	0.26
1/9	0.63	0.35	~0	~0	~0	~0	~0	~0

viscoelastoplastic studies for yield-stress increase, where only viscous yield-stress components were considered via a Papanastasiou regularisation (see López-Aguilar et al. 2015b).

Vortex dynamics results: (b) De Souza model, yield stress τ_{0d}-variation

In Fig. 5a, counterpart De Souza streamlines are displayed at different levels of yield-stress $\tau_{0d} = \{0.02, 0.2, 0.5, 1.0\}$ and elasticity $Wi = \{0.1, 1.0, 5.0, 10.0\}$, alongside vortex intensity values in Table 2 and *upstream–downstream* vortex-intensity trend graphs in Fig. 5b–e. Note in particular here that results are analysed: (i) under τ_{0d}-variation at fixed Wi and (ii) with Wi-variation at fixed τ_{0d}. Conspicuously, both τ_{0d}-elevation and Wi-elevation promote vortex activity, *upstream*: via enhancement in strength and growth in size; *downstream*: via suppression in strength and shrinkage in size.

With *τ_{0d}-increase at fixed $Wi = 1.0$*, and in contrast to NM_τ_p_ABS response, De Souza *upstream* vortex dynamics are now not suppressed with τ_{0d}-increase, but to the contrary are *notably enhanced*. Indeed, the upstream vortex is significantly enlarged and more active at $\tau_{0d} = \{0.02, 0.2, 0.5, 1.0\}$ (see Table 2, Fig. 5b). Furthermore, the downstream vortex continually shrinks as τ_{0d} is elevated, and consistently appears significantly smaller than its counterpart upstream vortex. Such upstream vortex enhancement and downstream vortex suppression may be correlated with the larger N_{1Shear}-response with τ_{0d}-rise at fixed-Wi level (Fig. 2d). As such and through τ_{0d}, this asymmetric response about the contraction may be associated with the influence of plasticity. Moreover, note at $Wi = 5$, the latter stages of *τ_{0d}-increase* between $\tau_{0d} = \{0.5, 1.0\}$, reveal a rapid decline in downstream vortex intensity (see Fig. 5c).

Moreover, at *fixed $\tau_{0d} = 0.2$ and under Wi-rise*, the elastic asymmetries stimulated are more exaggerated than noted above under NM_τ_p_ABS($\beta = 0.9$). Here, as Wi-rises, upstream vortices become dramatically larger, more intense and more concave; whilst counterpart downstream vortices show more extreme trends in shrinkage. These asymmetries in upstream–downstream vortices may be associated with the pronounced trend in rising N_{1Shear} with increasing shear rate in pure shear flow (Fig. 2d). Notably, with still further elevation in τ_{0d}-value, the downstream vortex practically disappears at $\{\tau_{0d} = 1.0,\ Wi = 5\}$. Then, consistently and with τ_{0d}-rise, this downstream vortex removal may be correlated with the larger N_{1Shear}-local-maximum (Fig. 2d). In addition, in the specific range $\{0.02 \leq \tau_{0d} \leq 0.5;\ 5 \leq Wi \leq 10\}$, even downstream vortex enhancement is noted. Such trends are clearly depicted in the plots Fig. 5b–e.

Yield fronts: yielded–unyielded regions, first normal stress difference N_1

Considering the magnitude and influence of yield stress, it is instructive to examine the division between yielded and unyielded regions. To this end, yield fronts are provided in Fig. 6a for NM_τ_p_ABS solutions, and in Fig. 6b for De Souza solutions. Here, the yield-stress cut-off criterion is based on the magnitude of stress (derived from its second invariant) falling below the yield stress. In addition, counterpart N_1-fields are provided in Fig. 7, again per model.

Effective yield-stress τ_{0eff}-elevation

At relatively *low yield-stress levels* with {NM_τ_p_ABS($\beta = 0.9$), De Souza($\tau_{0d} = 0.2$)}, both NM_τ_p_ABS data in Fig. 6a (top-row) and De Souza data in Fig. 6b (second-row down), display a single red-yielded X-shaped region. Such regions are interconnected throughout the flow-domain across the full range of Wi-values considered. This flowing-region is impinged upon by central blue-unyielded regions, located upstream and downstream of the contraction. There are additional relatively smaller unyielded regions confined in the recess zones, roughly corresponding to the recirculation zones identified above. The shape of these recess zones differs with model solution, so that NM_τ_p_ABS provides convex unyielded regions, whilst De Souza response is concave (relative to the salient corner). Consistently, with a relatively lower yield stress of De Souza($\tau_{0d} = 0.02$), in the top-row of Fig. 6b, the fields mostly contain yielded material. Here, slender upstream and downstream blue-unyielded regions are apparent, located at the longitudinal axis on the flow centreline. Moreover, there are some hints of small blue-unyielded regions to be observed in the upstream and downstream recess corners. With Wi-rise, these isolated solid regions appear detached from the walls and become asymmetrical about the axis in the contraction plane. Switching attention next to N_1-field data and under these relatively less demanding flow conditions, NM_τ_p_ABS N_1-fields of Fig. 7a (top-row, $\beta = 0.9$) display a small yellow-positive

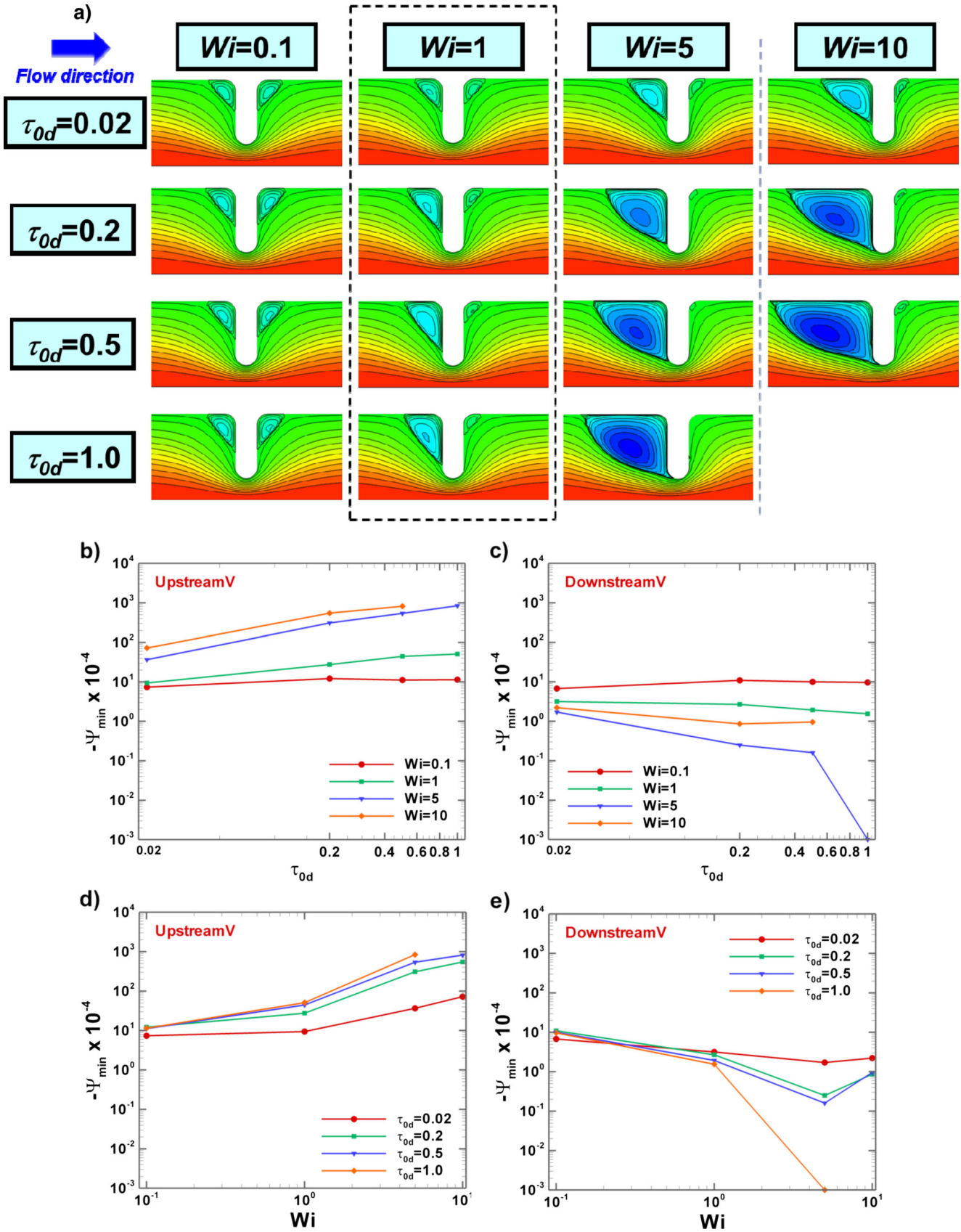

Fig. 5 Streamlines and vortex intensity against τ_{0d} and Wi; De Souza $\{K, n, \dot{\gamma}_{0d}, \beta, \omega_{DS}\} = \{0.1, 0.5, 0.3, 1/9, 1.0\}$ τ_{0d}-variation $\tau_{0d} = \{0.02, 0.2, 0.5, 1.0\}$

Table 2 Vortex intensity ($\Psi_{min} = -\Psi_{min}^{*}\, x10^{-4}$) against τ_{0d} and Wi; De Souza $\{\beta, K, n, \dot{\gamma}_{0d}, \omega_{DS}\} = \{1/9, 0.1, 0.5, 0.3, 1.0\}$

	$\Psi_{min} = -\Psi_{min}^{*}\, x10^{-4}$							
	$Wi = 0.1$		$Wi = 1.0$		$Wi = 5.0$		$Wi = 10.0$	
τ_{0d}	Ups	Dns	Ups	Dns	Ups	Dns	Ups	Dns
0.02	7.37	6.78	9.43	3.17	36.67	1.71	72.38	2.21
0.2	12.18	10.95	27.44	2.69	309.75	0.25	548.58	0.86
0.5	11.17	10.06	44.30	1.93	540.08	0.16	817.24	0.96
1.0	11.44	9.70	50.83	1.55	840.75	~0	–	–

region (symmetric about the centreline), mainly confined within the contraction-gap $\forall Wi$. In contrast in Fig. 7b (top-row, $\tau_{0d} = 0.02$), De Souza N_1-fields commence from relatively small symmetrical (now about contraction plane, centreline) non-zero N_1-regions at $Wi = 0.1$. This difference in the N_1-intensity may be correlated with the solvent-fraction level strategy per model, decreasing for NM_τ_p_ABS solutions and fixed for De Souza data. Top-row NM_τ_p_ABS-data in Fig. 7a illustrate solvent-dominated $\beta = 0.9$ conditions, whilst De Souza solutions belong to a higher polymer-concentration conditions of $\beta = 1/9$.

As the effective *yield-stress* τ_{0eff} *is increased*, either by NM_τ_p_ABS(β-decrease) of Fig. 6a, or De Souza(τ_{0d}-increase) in Fig. 6b, the blue-unyielded regions expand outwards and space-occupy the whole upstream and downstream flow sections, reaching the bounding pipe walls and engulfing the recess zones. In both solutions, this isolates a trapped red-yielded region within and about the contraction-gap alone, which shrinks with increasing τ_{0eff}. The shape of this red-yielded gap-region is again model-solution dependent. This is one of a symmetrical-about-centreline split-doughnut form

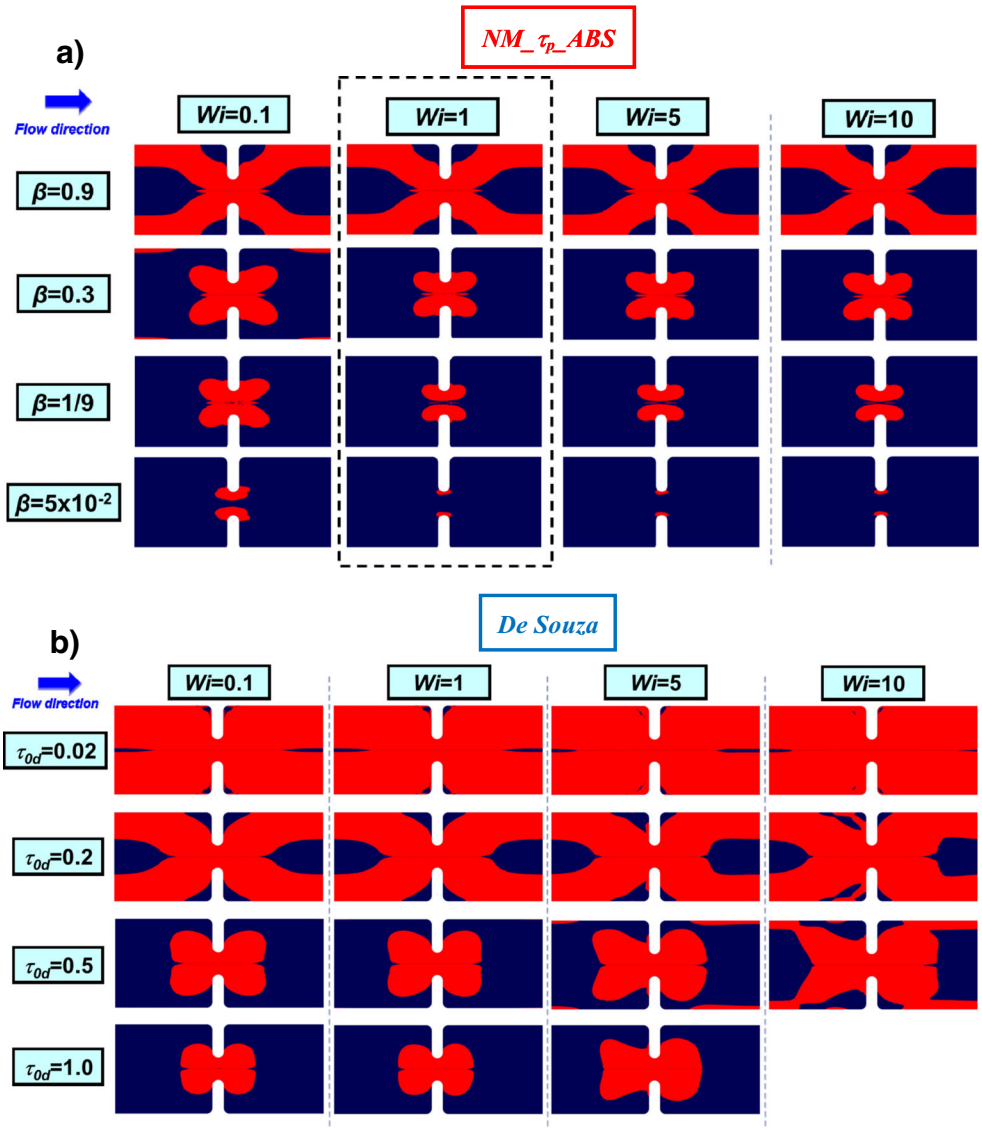

Fig. 6 Yield fronts against τ_{0eff} and Wi. **a** NM_τ_p_ABS $\{\omega, \xi_{G0}\} = \{4.0, 1.0\}$ β-variation $\beta = \{0.9, 0.3, 1/9, 5 \times 10^{-2}\}$. **b** De Souza $\{K, n, \dot{\gamma}_{0d}, \beta, \omega_{DS}\} = \{0.1, 0.5, 0.3, 1/9, 1.0\}$ τ_{0d}-variation $\tau_{0d} = \{0.02, 0.2, 0.5, 1.0\}$

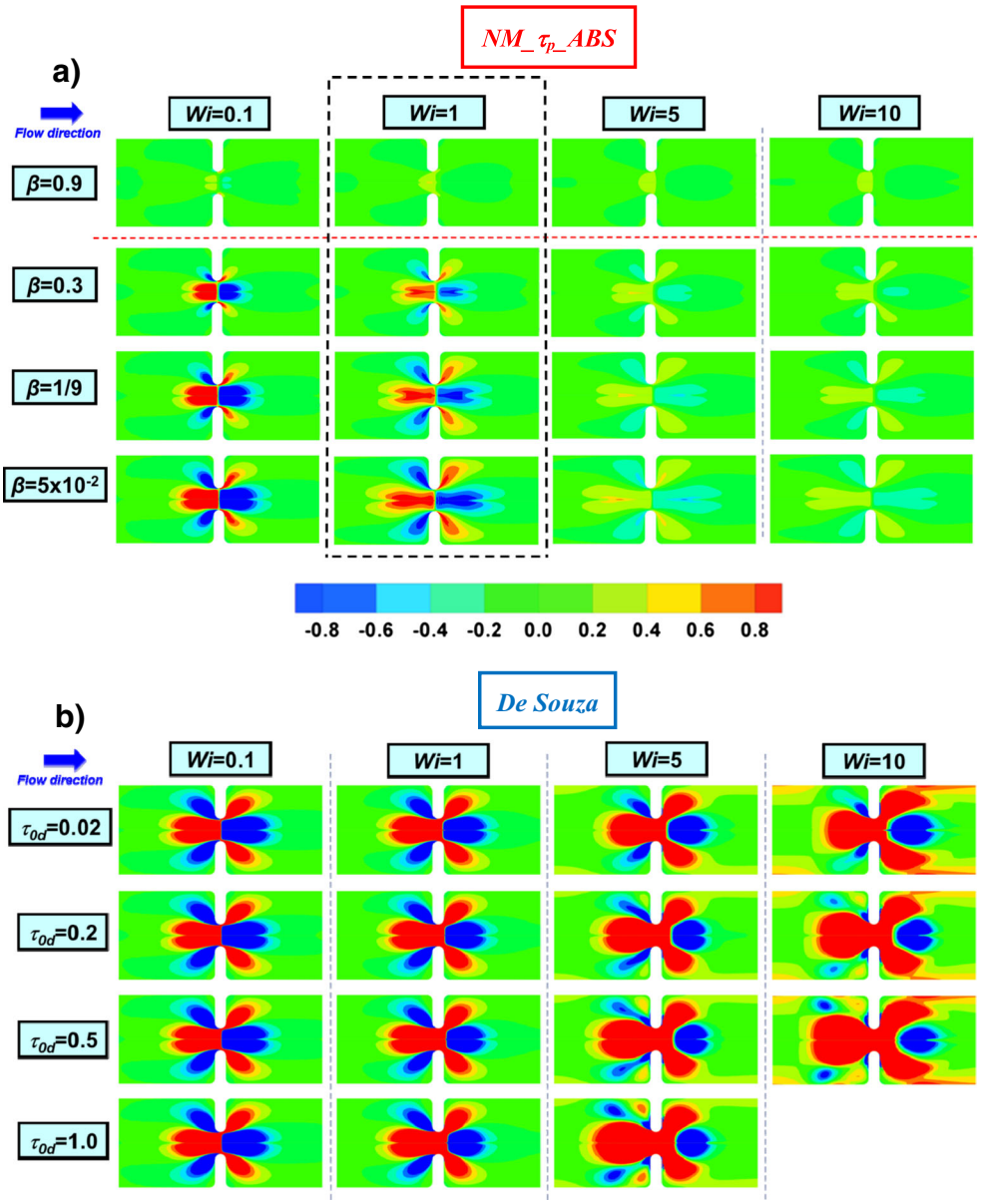

Fig. 7 N_1 against τ_{0eff} and Wi. **a** NM_τ_p_ABS $\{\omega, \xi_{G0}\} = \{4.0, 1.0\}$ β-variation $\beta = \{0.9, 0.3, 1/9, 5 \times 10^{-2}\}$. **b** De Souza $\{K, n, \dot{\gamma}_{0d}, \beta, \omega_{DS}\} = \{0.1, 0.5, 0.3, 1/9, 1.0\}$ τ_{0d}-variation $\tau_{0d} = \{0.02, 0.2, 0.5, 1.0\}$

for NM_τ_p_ABS(β-decrease). Its wings are symmetrical about the contraction plane, which shrink with increasing τ_{0eff}, as the narrow blue-unyielded centreline-band of material expands. Finally, by $\beta = 5 \times 10^{-2}$, these flowing regions have dramatically shrunk to those around the contraction-tip alone, so that they have almost disappeared. In contrast for De Souza(τ_{0d}-increase), the red-yielded gap-region shape is one of a four-leaf clover (shamrock-like), that contracts with increasing τ_{0eff}. NM_τ_p_ABS N_1-fields under β-decrease and fixed-Wi (Fig. 7a, $Wi = 1$), now provide significant growth with increasing τ_{0eff}, in size and intensification, into eight-winged butterfly patterns, symmetrical about the centreline and anti-symmetrical about the contraction plane. Rheologically, this growth increase, in size and intensification, may be correlated through β-decrease, with the rise in τ_{0eff}, N_{1shear}-, η_{Shear}- and η_{Ext}-plateaus in the material functions (Fig. 2a, b and Fig. 3a, b). In comparison, De Souza N_1-fields under τ_{0d}-increase (Fig. 7b, $Wi = \{0.1, 1\}$), now render only intensification of the non-zero N_1-regions, without the accompanying space expansion of NM_τ_p_ABS. Here, the absence of apparent growth in N_1-patterns, with τ_{0d}-rise at fixed and low $Wi = \{0.1, 1\}$, may be attributed to the constancy in first-plateaux of η_{Shear}- and η_{Ext}- across the low-deformation rate regime (Fig. 3c, d). Moreover at fixed-$Wi = \{5, 10\}$, some degree of growth and asymmetry (about the contraction-plane) is observed with τ_{0d}-rise in the crab-like N_1-patterns (Fig. 7b). With τ_{0d}-rise at fixed-$Wi = \{5, 10\}$, these size-growth and asymmetric features may be associated with the

increasing N_{1Shear}- and τ_{rz}-levels at equivalent fixed shear rates in material functions (Fig. 2d). Unfortunately, numerical solution for $Wi=10$ and $\tau_{0d}=1$ was unattainable due to lack of tractability under this more severe setting (Fig. 7b). As noted earlier, η_{Ext}-data for $\tau_{0d}=1$ is the only instance to provide pronounced strain-hardening features at moderate rates (Fig. 3d).

Elasticity *Wi*-elevation

In the NM_τ_p_ABS yield fronts of Fig. 6a, the ($Wi=0.1$)-dataset yielded-regions appear relatively larger in space-occupation, with respect to the dataset at $Wi=1$. In addition, N_1-fields at $Wi=0.1$ display relatively smaller and more intense patterns than those at $Wi=1$. These $Wi=1$ patterns appear larger but less intense (Fig. 7a). This N_1-growth in space occupation correlates through shear-rate elevation, with the N_{1Shear}- and τ_{rz}-rising response at low shear rates (Fig. 2a, b). The intensity loss may be accounted for through deformation-rate rise, and the drop in η_{Shear}- and η_{Ext}-data of Fig. 3a, b, from their corresponding low-deformation-rate plateau-values. The drop in η_{Shear}-data is a consequence of the prevailing *shear-thinning* (effective in the strong-shear zone about the contraction tip); whilst the drop in η_{Ext}-data is due to the impact of *strain-softening* (effective in the strong-extensional zone about the gap centre, at centreline). Yield-front fixed-β datasets in the range $1\leq Wi\leq 10$ of Fig. 6a prove invariant with *Wi*-rise and at any β-setting. Consistently, counterpart N_1-fields (Fig. 7a) reflect the symmetrical butterfly-like patterns about the contraction plane, which lose intensity with *Wi*-rise, but retain shape–size. The constancy of size of the symmetrical butterfly-like patterns, in the range $1\leq Wi\leq 10$ of Fig. 2b, may be associated with the attainment of the N_{1Shear}-plateau levels. Moreover, the continual loss of intensity with *Wi*-rise, is due to both shear-thinning and strain-softening properties (Fig. 3a, b).

In contrast to the foregoing, De Souza yield fronts (Fig. 6b) and corresponding N_1-fields (Fig. 7b), become asymmetrical about the contraction as *Wi* rises, a distinct elastic response with display of downstream convection. This phenomenon is illustrated in De Souza N_1-fields, which dramatically change from symmetrical patterns at relatively small τ_{0d} and *Wi* levels (Fig. 7b), to asymmetrical crab-like positive-regions with satellite blue-negative spots for $Wi\geq 5.0$ and $\tau_{0d}\geq 0.5$. The upstream–downstream asymmetry and intensification of fan-like wings about the contraction tip (shear-dominated zone) with *Wi*-rise, may be correlated with the *rise in viscometric* N_{1Shear}-response (see Fig. 2d); whilst the downstream convection and asymmetry it creates may be associated with extensional influence from *strain-softening*-response about the gap centre near the centreline. Likewise, there is significant De Souza yield-front response (Fig. 6b) at $\tau_{0d}=0.5$, across the range $0.1\leq Wi\leq 10$. There, the $Wi=0.1$ symmetrical yielded-region

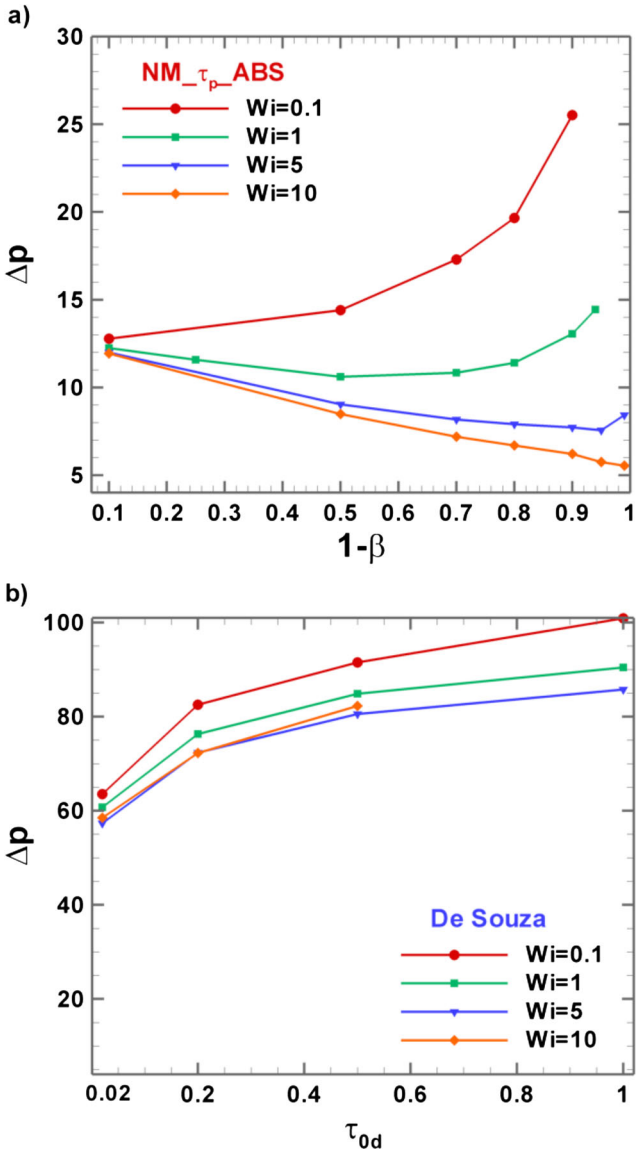

Fig. 8 Total pressure drop against *Wi*; NM_τ_p_ABS(β-decrease) {ω, ξ_{G0}} = {4.0, 1.0}, De Souza(τ_{0d}-increase) {K, n, $\dot{\gamma}_{0d}$, β, ω_{DS}} = {0.1, 0.5, 0.3, 1/9, 1.0}

Table 3 Total pressure drop (Δp) against β and *Wi*; NM_τ_p_ABS {ω, ξ_{G0}} = {4.0, 1.0}

	Δp			
β	$Wi=0.1$	$Wi=5.0$	$Wi=1.0$	$Wi=10.0$
0.9	12.78	12.25	11.99	11.94
0.5	14.41	10.61	9.04	8.48
0.3	17.29	10.84	8.17	7.19
0.2	19.66	11.41	7.91	6.70
1/9	25.52	13.05	7.72	6.21
0.05	–	14.44*	7.56	5.75
0.01	–	–	8.43	5.54

*$\beta=0.06$

Table 4 Total pressure drop (Δp) against τ_{0d} and Wi; De Souza $\{\beta, K, n, \gamma_{0d}, \omega_{DS}\} = \{1/9, 0.1, 0.5, 0.3, 1.0\}$

	Δp			
τ_{0d}	$Wi = 0.1$	$Wi = 5.0$	$Wi = 1.0$	$Wi = 10.0$
0.02	63.54	60.75	57.33	58.50
0.2	82.53	76.32	72.36	72.27
0.5	91.53	84.87	80.55	82.26
1.0	100.89	90.45	85.77	–

gap-pattern, gives way to the $Wi = 5$ central gap pattern. At $Wi = 5$, elastic asymmetry is observed in the yielded regions about the contraction plane, with a mushroom-like shape downstream, and a fish-tail-like shape upstream, both expanding with Wi-rise. This effect is also translated to solution at $\{\tau_{0d} = 1, Wi = 5\}$, but with excessive squeezing up towards the contraction plane. As noted above and at any fixed Wi-level, yielded regions are consistently suppressed with rise in τ_{0d}. Moreover, at $\tau_{0d} = 0.5$ and across the range $5 \le Wi \le 10$, a new predominantly unyielded-zone feature begins to appear upstream and downstream of the contraction, where red-yielded regions appear attached to the walls at $Wi = 5$, and which at $Wi = 10$, connect up with the central red-yielded region downstream mushroom-headed and upstream fish-like-tail, thus forming oddly-shaped blue-unyielded regions that elongate downstream from the upstream recess corners.

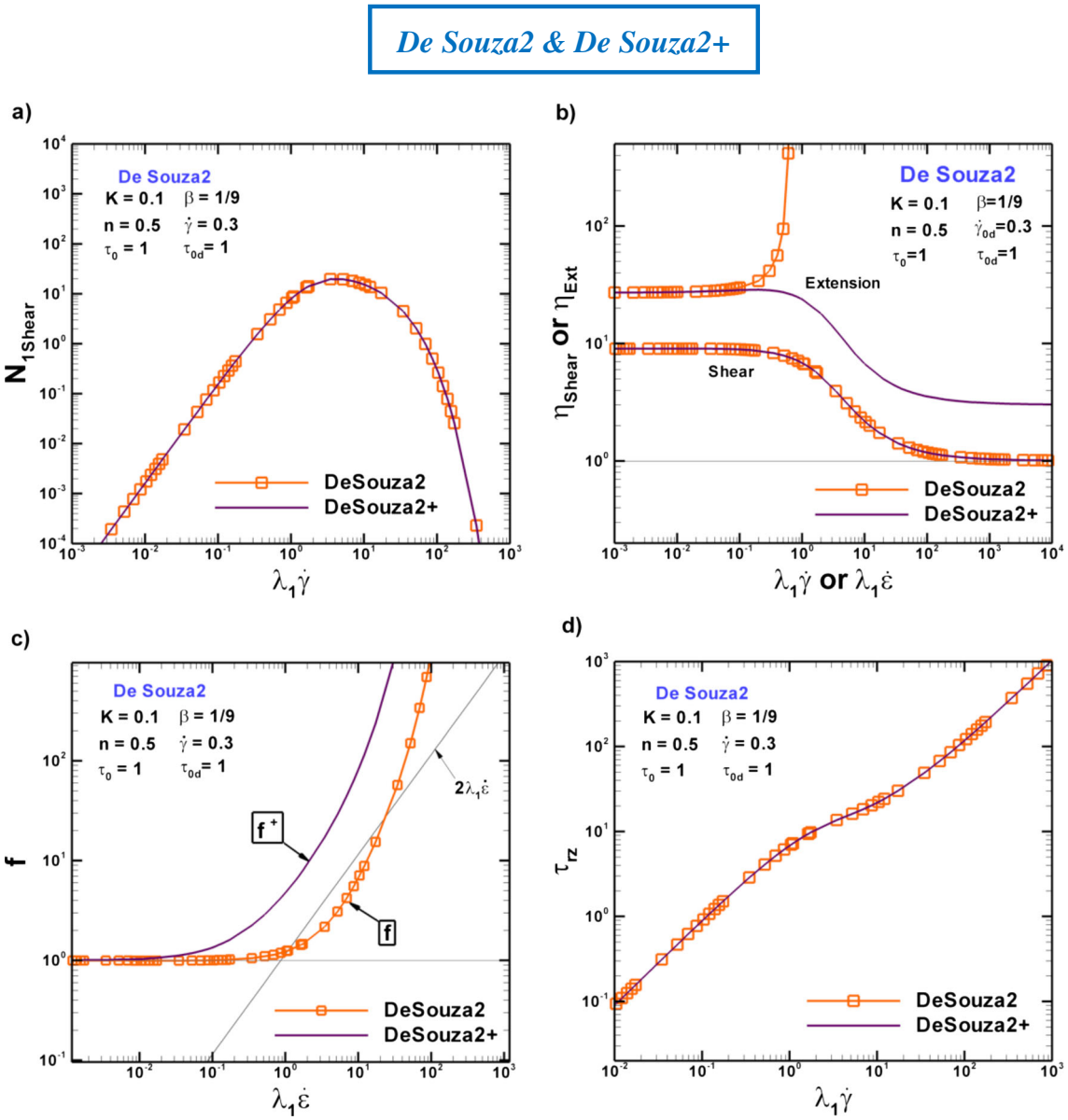

Fig. 9 **a** $N_{1\text{Shear}}$, **b** η_{Ext}, **c** f-functional, and **d** τ_{rz} against deformation-rate. De Souza2 vs De Souza2+; $\{K, n, \dot{\gamma}_{0d}, \tau_0, \tau_{0d}, \beta, \omega_{DS}\} = \{0.1, 0.5, 0.3, 1.0, 1.0, 1/9, 1.0\}$

Total pressure-drop results

In Fig. 8a (Table 3), the NM_τ_p_ABS total pressure drop Δp is plotted against polymeric fraction (1-β), representing data curves for $Wi = \{0.1, 1.0, 5.0, 10.0\}$. With Wi-rise, the Δp-level drop at any fixed polymer concentration, thus reflecting enhanced elasticity effects that broaden with increase in polymer concentration. At one extreme of fixed $Wi = 0.1$, where diffusive forces dominate elastic forces, the Δp data curve follows a *monotonically rising* trend from $\{1\text{-}\beta, \Delta p\} \sim \{0.1, 12.75\}$ up to $\{1\text{-}\beta, \Delta p\} \sim \{8/9, 20.0\}$. At the other fixed extreme of $Wi = 10.0$, Δp response follows a *monotonically declining* trend from $\{1\text{-}\beta, \Delta p\} \sim \{0.1, 11.9\}$ to $\{1\text{-}\beta, \Delta p\} \sim \{0.99, 5.5\}$. Intermediate states are extracted in-between.

The equivalent De Souza total pressure drop Δp is plotted against τ_{0d}-rise in Fig. 8b (Table 4). Note here that the pressure-drop levels are somewhat higher than those obtained under NM_τ_p_ABS (across all four Wi–instances). Here, only monotonic rise is gathered with τ_{0d}-increase for each value of Wi, as noted against NM_τ_p_ABS findings under polymeric-fraction (1-β) increase. Generally, Δp-levels drop with Wi-rise at any particular τ_{0d}-value; as observed likewise for NM_τ_p_ABS(Δp, fixed β).

Conclusions

Viscoelastoplastic solutions have been extracted through two thixotropic constitutive models, NM_τ_p_ABS and De Souza models, where each adopts a different approach to introduce plastic response. First, NM_τ_p_ABS yield-stress features are analysed under solvent-fraction β-decrease, according to polymer concentration increase. Then, second, counterpart De Souza predictions are studied, under dynamic (τ_{0d}) and static (τ_0) yield-stress variation.

In these solutions, significant differences have been observed in *vortex dynamics*. First, for NM_τ_p_ABS with solvent-fraction β-decrease and elasticity Wi-increase, vortex suppression is generally observed with no asymmetry about the contraction. That is, even to the point of being visually absent. Second, De Souza vortex activity is stimulated and grows asymmetrical, with either yield-stress $\tau_{0\text{eff}}$ increase or elasticity Wi-increase. Consistently, in viscometric flows, NM_τ_p_ABS reflects a relatively more drastic response to solvent fraction β-variation: with larger NM_τ_p_ABS $\tau_{0\text{eff}}$-, $N_{1\text{Shear}}$-, low-deformation-rate η_{Shear} and η_{Ext} plateaux; as opposed to that of De Souza with τ_{0d}-variation, which only provides elevation in τ_{0eff}- and N_{1Shear}-response. Here, NM_τ_p_ABS τ_{rz}-curves provide a flatter and wider response (three orders of magnitude at maximum) in its non-linear range, alongside larger τ_{0eff}-values with β-decrease. In contrast, De Souza data curves have a fixed width at each τ_{0d}-level (one and a half orders-of-magnitude), which gradually shifts to larger values with τ_{0d}-increase. These characteristic features are reflected in *first normal stress-difference N_1-fields and yield fronts*. Here, NM_τ_p_ABS with β-decrease ($\tau_{0\text{eff}}$-elevation), provides intensification and growth of non-zero N_1-regions, and confinement of yielded regions about the contraction.

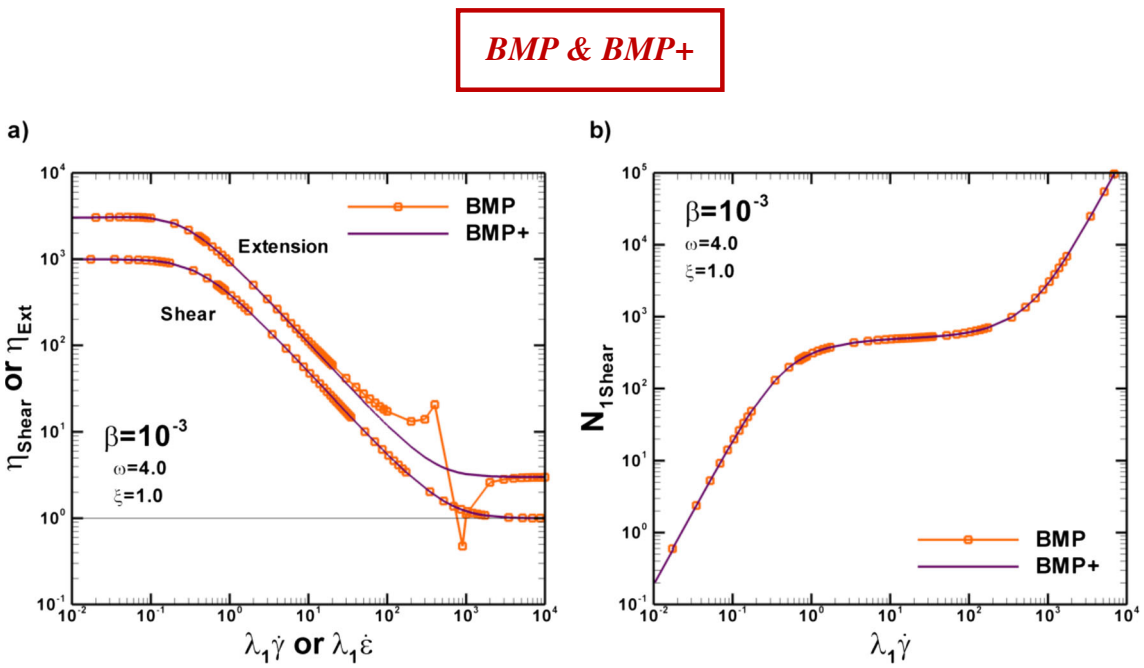

Fig. 10 η_{Shear}, η_{Ext} and $N_{1\text{Shear}}$ and against deformation-rate; BMP vs BMP+; $\{\omega, \xi_{G0}, \beta\} = \{4.0, 1.0, 10^{-3}\}$

With *Wi*-rise, the initial size-growth and further size-constancy of non-zero N_1-regions, correlates with pattern change in simple-shear $N_{1\text{Shear}}$ under shear-rate rise. Viscometric $N_{1\text{Shear}}$ first rises at low shear rates, and then finally plateaus at large rates. In addition, the intensity of these symmetrical butterfly-like N_1-regions diminishes with *Wi*-increase, due to prevailing shear-thinning and strain-softening influence. Conspicuously, for NM_τ_p_ABS, no asymmetry is recorded in N_1-data and yield fronts, as viscoelasticity (through *Wi*) or plasticity (through β) are increased. In contrast, De Souza solutions reveal N_1-intensification and confinement with τ_{0d}-increase, in accordance with its rising $N_{1\text{Shear}}$-response. In addition and through *Wi*-rise, asymmetries are observed as viscoelasticity is emphasised, through crab-like N_1-fields and mushroom-like yielded-regions.

In the micellar NM_τ_p_ABS solutions, there are distinct effects in *total pressure drop* (Δp) with polymeric-fraction (1-β)-increase and *Wi*-rise. At low extremes of fixed $Wi = 0.1$, Δp rises monotonically with polymer concentration, whilst at larger levels of fixed $Wi = 10$, Δp declines. In contrast, De Souza Δp-solutions under τ_{0d}-rise and for fixed *Wi*, provide a simpler but relatively larger response in magnitude, where only a monotonic rising trend is recorded. Furthermore, with *Wi*-rise and at any fixed $\tau_{0\text{eff}}$-level, De Souza Δp-solutions agree in declining trend with those of NM_τ_p_ABS.

Acknowledgments Financial support (scholarship to J.E.L.-A.) from Consejo Nacional de Ciencia y Tecnología (CONACYT, México), Zienkiewcz College of Engineering scholarship and NHS-Wales AbertaWi Bro Morgannwg Trust-fund, is gratefully acknowledged.

Appendix A—reformulation of De Souza model

More recently, a reformulated model (De Souza2) has appeared (De Souza and Thompson 2013), through changes given in the definitions for $G_s(\lambda)$, $\eta_p(\lambda)$, λ_{ss}, $\boldsymbol{\tau}_p$ and λ. The theoretical benefits claimed for this model lie in its ability to reflect both '*apparent*' and '*true*' yield stress functionality, via its representation of shear viscosity at low shear rates. 'True' yield stress refers to a material for which $\eta_{p0} \to \infty$ and, hence, $\lambda_0 \to \infty$; whilst for fluids with an 'apparent' yield stress, η_{p0} and λ_0 are large but finite (De Souza and Thompson 2013). Then, the corresponding De Souza2 dimensionless identities and equations now become:

$$\frac{G_s(\lambda)}{G_0} = e^{\left[m\left(\frac{1}{\lambda}-\frac{1}{\lambda_0}\right)\right]}, \tag{A.1}$$

$$\eta_p(\lambda) = e^{\lambda}-1, \tag{A.2}$$

$$\lambda_{ss}(II_{\boldsymbol{D}}) = \ln\eta_{ss}(II_{\boldsymbol{D}}), \tag{A.3}$$

$$Wi\overset{\nabla}{\boldsymbol{\tau}}_p = 2\Gamma e^{m\left(\frac{1}{\lambda}-\frac{1}{\lambda_0}\right)}\boldsymbol{D}-f\boldsymbol{\tau}_p, \tag{A.4}$$

$$\left(\frac{\partial}{\partial t}+\boldsymbol{u}\cdot\nabla\right)\lambda = \frac{1}{\omega_{DS}}\left[\left(\frac{1}{\lambda}-\frac{1}{\lambda_0}\right)^a-\left(\frac{\lambda}{\lambda_{ss}}\right)^b\left(\frac{1}{\lambda_{ss}}-\frac{1}{\lambda_0}\right)^a\right]. \tag{A.5}$$

The material functions for this model are provided in Fig. 9 under $\tau_{0d} = 1$, where $f = \left\{\frac{\eta_{p0}}{\eta_p}\exp\left[m\left(\frac{1}{\lambda}-\frac{1}{\lambda_0}\right)\right]\right\}$. With respect to the primary De Souza model (Fig. 2c, d and Fig. 3c, d), De Souza2 $N_{1\text{Shear}}$- and η_{Ext}-data are the only components that differ. Notably and at high shear rates, De Souza2 $N_{1\text{Shear}}$-data provides declining trends (Fig. 9a), so that elastic effects will be lost. Furthermore, in De Souza2 η_{Ext}-data, there is evidence of unbounded extensional response at a finite strain-rate of $\lambda_1\dot{\varepsilon} \sim 0.6$ (Fig. 9b). In the present complex flow, these singularities in extensional viscosity predictions will stimulate early numerical-intractability. Moreover with *Wi*-rise, $N_{1\text{Shear}}$-declining trends at high deformation-rates will generate shrinking non-zero N_1-regions (yielded stress zones), with loss of intensity and upstream-vortex suppression. Hence, counterpart De Souza2 solutions are not anticipated to display any further interesting and increased elastic effects, but more closely reflect the solution response for NM_τ_p_ABS.

To avoid extensional viscosity singularities, a revision of De Souza2 in the form of De Souza2+ f^+-functional, may be derived as follows. Passing first through the analysis for the uniaxial extensional viscosity pole ($f-2\lambda_1\dot{\varepsilon}$) under De Souza2 viz.:

$$\left(f-2\lambda_1\dot{\varepsilon}\right) = \frac{\eta_{p0}}{\eta_p}\exp\left[m\left(\frac{1}{\lambda}-\frac{1}{\lambda_0}\right)\right]-2\lambda_1\dot{\varepsilon}, \tag{A.6}$$

and observing that this quantity must remain positive (i.e. $f-2\lambda_1\dot{\varepsilon} > 0$) to generate finite extensional viscosity (so, f must not cross the value of $2\lambda_1\dot{\varepsilon}$). Rearranging Eq. (A.6) under this restriction, one may gather:

$$\left(\frac{1}{(2\lambda_1\dot{\varepsilon})}\right)f > 1. \tag{A.7}$$

From Eq. (A.7), one can extract valuable information to define a more suitable f-functionality. Note in this case, that the inequality in (A.7) may be violated when:

$2\lambda_1\dot{\varepsilon} > f$ and > 0 (so, with rising $\lambda_1\dot{\varepsilon}$).

Normally, one might expect that $f \geq 1$, which is true for these shear-thinning materials, as here.

Assuming $\lambda_1\dot{\varepsilon} \geq 0$, by considering only rate magnitude, and by extraction of a factor with $(2\lambda_1\dot{\varepsilon})$, then one may propose the alternative functional form (f^+) [3]:

$$f^+ = (1 + 2\lambda_1\dot{\varepsilon})f. \tag{A.8}$$

Then, considering what is necessary to satisfy the pole-avoidance condition $(f^+ - 2\lambda_1\dot{\varepsilon}) > 0$, this implies that

$\{f(1 + 2\lambda_1\dot{\varepsilon}) - 2\lambda_1\dot{\varepsilon}\} > 0$, or simply, $\{f + 2\lambda_1\dot{\varepsilon}(f-1)\} > 0$.

Such a condition can be met, independently of $2\lambda_1\dot{\varepsilon}$ (so also, rate), whilst:

$$f \geq 1 \rightarrow (f-1) \geq 0\,,$$

a base and standard requirement to be satisfied by the *f*-functional. This holds here for De Souza2 shear-thinning models (and even Oldroyd-B for that matter). Clearly, such adjustment in standard forms of *f*-functional may be applied equally in more general constitutive context, with the objective of achieving boundedness in extensional response.

The consequences of such a correction are reflected in the trends of uniaxial extension *f*-functional against strain rate of Fig. 9c. Here, it is demonstrated that, as opposed to De Souza2, De Souza2+ f^+-functional data do not meet the extensional-viscosity pole of $(f - 2\lambda_1\dot{\varepsilon})$. Accordingly, finite extensibility is observed for De Souza2+, as illustrated in the extensional viscosity trends of Fig. 9b. Conspicuously, DeSouza2 η_{Ext} locates unboundedness at smaller extension rates, whilst De Souza2+ displays pronounced strain-softening features. Moreover, it is noteworthy that such correction only becomes active in flow situations with extensional deformation ($\dot{\varepsilon} > 0$), and therefore is rendered non-contributory in pure-shear flow (see $N_{1\mathrm{Shear}}$ and τ_{rz} –data in Fig. 9a and d). Unfortunately, in this form, $N_{1\mathrm{Shear}}$ does not supply an ultimate upturn, as desired for enhanced elastic effects (Fig. 9a) (see comments in Appendix B below under BMP+). Pursuit of $N_{1\mathrm{Shear}}$ ultimate upturn is left to further study under the De Souza2+ formulation.

Appendix B—reformulation of BMP model

Within the framework of Eq. (3)–(5), a micellar model capable of providing ultimate rise in $N_{1\mathrm{Shear}}$ with shear rate is that of Bautista et al. 1999 (BMP-version):

$$\left(\frac{\partial}{\partial t} + \boldsymbol{u}\cdot\nabla\right)f = \frac{1}{\omega}(1-f) + \xi\left(\frac{\eta_{p0}}{\eta_\infty} - f\right)\boldsymbol{T} : \boldsymbol{D}. \tag{B.1}$$

[3] Note that this alternative f^+-form may be written in general-flow notation, taking $\dot{\varepsilon} = \left(3\frac{III_D}{II_D}\right)$ and $k = 2$ (under uniaxial extension), as: $f^+ = \left[1 + k\left(3\frac{III_D}{II_D}\right)\lambda_1\right]f$. Here, II_D and III_D are the second and third invariants of **D**, respectively.

In this form, the destruction term now accommodates the *f*-functional as well, where $f = (\eta_{p0}/\eta_p)$. Here, $\xi = k\eta_s\frac{U}{L}$ is the corresponding dimensionless destruction parameter. Notably, alongside providing a high shear-rate upturn in $N_{1\mathrm{Shear}}$ (Fig. 10b), this model also predicts unbounded extensibility at finite rates, when the *f*-functional attains the value $\frac{\eta_{p0}}{\eta_\infty}$ (Fig. 10a, when η_p reaches η_∞). To make progress at the time of creation for the BMP-version and to overcome the deficiency in extensional response, Boek et al. 2005 suggested to simply discard the *f*–contribution to the destruction term (generating the so-called MBM model). Unfortunately, this practice had the drawback of also suppressing the high shear-rate upturn in $N_{1\mathrm{Shear}}$.

An alternative approach to recapture boundedness in extensional viscosity, whilst retaining ultimate upturn in $N_{1\mathrm{Shear}}$, which produces a revision of BMP in the form of BMP+, may be conceived as follows. The *f*-functional may be amended for use in Eq. (B.1), then replacing *f* with the new form $f^+ = \frac{\eta_{p0}}{\eta_p + \eta_\infty}$, (BMP+). Here the shift, provided in the denominator of f^+ with η_∞, avoids the otherwise null factor clash at the second-Newtonian plateau. One notes that the inverse of the factor $\left(\frac{\eta_{p0}}{\eta_\infty} - f^+\right)$ also appears in the expression for extensional-viscosity. Hence, finite extensibility is recovered under BMP+ (Fig. 10a), with no change in η_{Shear}- and $N_{1\mathrm{Shear}}$-response. Hence, the ultimate upturn in $N_{1\mathrm{Shear}}$ is ensured, as desired for sustained elastic response.

One notes that these new model-variants, as described in Appendix A (De Souza2+) and Appendix B (BMP+), are currently being implemented in complex flow, for corresponding findings to be published subsequently.

References

Aboubacar M, Matallah H, Tamaddon-Jahromi HR, Webster MF (2002a) Numerical prediction of extensional flows in contraction geometries: hybrid finite volume/element method. J Non-Newton Fluid Mech 104:125–164

Aboubacar M, Matallah H, Webster MF (2002b) Highly elastic solutions for Oldroyd- B and Phan-Thien/Tanner fluids with a finite volume/element method: planar contraction flows. J Non-Newton Fluid Mech 103:65–103

Aguayo JP, Tamaddon-Jahromi HR, Webster MF (2008) Excess pressure-drop estimation in contraction and expansion flows for constant shear-viscosity, extension strain hardening fluids. J Non-Newton Fluid Mech 153:157–176

Bautista F, de Santos JM, Puig JE, Manero O (1999) Understanding thixotropic and antithixotropic behavior of viscoelastic micellar solutions and liquid crystalline dispersions I The model. J Non-Newton Fluid Mech 80:93–113

Bautista F, Soltero JFA, Pérez-López JH, Puig JE, Manero O (2000) On the shear banding flow of elongated micellar solutions. J Non-Newton Fluid Mech 94:57–66

Belblidia F, Matallah H, Webster MF (2008) Alternative subcell discretisations for viscoelastic flow: velocity-gradient approximation. J Non-Newton Fluid Mech 151:69–88

Binding DM, Phillips PM, Phillips TN (2006) Contraction/expansion flows: the pressure drop and related issues. J Non-Newton Fluid Mech 137:31–38

Boek ES, Padding JT, Anderson VJ, Tardy PMJ, Crawshaw JP, Pearson JRA (2005) Constitutive equations for extensional flow of wormlike micelles: stability analysis of the Bautista-Manero model. J Non-Newton Fluid Mech 126:29–46

Calderas F, Herrera-Valencia EE, Sanchez-Solis A, Manero O, Medina-Torres L, Renteria A, Sanchez-Olivares G (2013) On the yield stress of complex materials. Korea-Aust Rheol J 25:233–242

de Souza PR (2009) Modeling the thixotropic behaviour of structured fluids. J Non Newton Fluid Mech 164:66–75

de Souza PR (2011) Thixotropic elasto-viscoplastic model for structured fluids. SoftMatter 7:2471–2483

de Souza PR, Thompson RL (2012) A critical overview of elasto-viscoplastic thixotropic behaviour modeling. J Non-Newton Fluid Mech 187–188:8–15

de Souza PR, Thompson RL (2013) A unified approach to model elasto-viscoplastic thixotropic yield-stress materials and apparent yield-stress fluids. Rheol Acta 52:673–694

Link FB, Frey S, Thompson RL, Naccache MF, de Souza PR (2015) Plane flow of thixotropic elasto-viscoplastic materials through a 1: 4 sudden expansion. J Non-Newton Fluid Mech 220:162–174

López-Aguilar JE, Webster MF, Tamaddon-Jahromi HR, Manero O (2014) A new constitutive model for worm-like micellar systems—numerical simulation of confined contraction-expansion flows. J Non-Newton Fluid Mech 204:7–21

López-Aguilar JE, Webster MF, Tamaddon-Jahromi HR, Manero O (2015a) High-Weissenberg predictions for micellar fluids in contraction-expansion flows. J Non-Newton Fluid Mech 222: 190–208

López-Aguilar JE, Webster MF, Tamaddon-Jahromi HR, Manero O (2015b) Numerical modelling of thixotropic and viscoelastoplastic materials in complex flows. Rheol Acta 54:307–325

Manero O, Bautista F, Soltero JFA, Puig JE (2002) Dynamics of worm-like micelles: the Cox-Merz rule. J Non-Newton Fluid Mech 106:1–15

Matallah H, Townsend P, Webster MF (1998) Recovery and stress-splitting schemes for viscoelastic flows. J Non-Newton Fluid Mech 75:139–166

Rothstein JP, McKinley GH (2001) The axisymmetric contraction–expansion: the role of extensional rheology on vortex growth dynamics and the enhanced pressure drop. J Non Newton Fluid Mech 98: 33–63

Walters K, Webster MF (2003) The distinctive CFD challenges of computational rheology. Int J Numer Meth Fluids 43:577–596

Wapperom P, Webster MF (1998) A second-order hybrid finite-element/volume method for viscoelastic flows. J Non-Newton Fluid Mech 79:405–431

Webster MF, Tamaddon-Jahromi HR, Aboubacar M (2005) Time-dependent algorithms for viscoelastic flow: finite element/volume schemes. Numer Meth Part Differ Eq 21:272–296

Yang J (2002) Viscoelastic wormlike micelles and their applications. Curr Opin Colloid Interface Sci 7:276–281